Computational Materials Science 215 (2022) 111769

Contents lists available at ScienceDirect

Computational Materials Science

journal homepage: www.elsevier.com/locate/commatsci

Letter

Activation energy of homogeneous nucleation of Zr hydride: Density functional theory calculation

Akio Ishii

Department of Mechanical Science and Bioengineering, Osaka University, 1-3 Machikaneyama-cho, Toyonaka, Osaka 560-8531, Japan

ARTICLE INFO

Keywords:
Zirconium hydride
Atomistic simulation
Density functional theory

ABSTRACT

Considering the nucleation process of Zr hydrides as phase transformation from hexagonal closed-packed (HCP) to face-centered tetragonal (FCT) structure, we calculated the activation energy of the homogeneous nucleation process of Zr hydrides and atomic rearrangement during nucleation for Zr_4H, Zr_2H, ZrH and ZrH_2 using density functional theory calculations and minimum energy path detection. At 0 K limit, although ZrH and ZrH_2 have lower chemical potentials and are more energetically stable than Zr_4H and Zr_2H, the latter have lower activation energies for nucleation. At finite temperatures, the crossover of activation energies occurs around 300 K, where ZrH becomes the most possible candidate with the lowest activation energy. This was explained by the difference in the atomic rearrangement and change in phonon frequency during phase transformation.

Zirconium (Zr) alloys are widely used as fuel claddings in nuclear reactors owing to their desirable properties. However, fuel claddings are constantly exposed to steam in a nuclear reactor, which inevitably infer hydrogen generation due to the oxidation of the Zr surface. Some of the generated hydrogen is absorbed by the Zr cladding and form Zr hydride precipitates [1,2], which usually reduce the ductility and fracture toughness of Zr alloys [2–5]. Therefore, understanding the mechanism of the Zr hydride nucleation is of key importance for maintaining the sustainability of fuel claddings in reactors. The experimentally observed Zr hydride precipitates were ζ (Zr_2H), γ (ZrH), δ ($ZrH_{1.66}$), and ϵ (ZrH_2) hydrides, the most common of which were γ and δ [1,3,6,7]. γ, δ, and ϵ hydrides have similar crystalline structures (i.e. face-centered tetragonal (FCT) or face-centered cubic (FCC)) whereas the matrix is hexagonal closed-packed (HCP) Zr (α Zr) [3,8]. The experimentally observed ζ (Zr_2H) hydride has an HCP structure [9], even though molecular dynamics (MD) simulations suggested the existence of a more stable FCT ζ hydride [10]. Despite experimental efforts to observe Zr hydrides, nucleation and transformation processes have remained unclear so far. This is mainly attributed to the fact that nucleation and transformation are caused by the rearrangement or shuffling of zirconium and hydrogen atoms, which is usually challenging to tackle using atomic-level dynamics or kinetics investigations.

On the other hand, atomistic simulations, such as molecular dynamics (MD) or density functional theory (DFT) simulations, are powerful tools for investigating atomic-level dynamics and discussing the kinetics energetically. However, to the best of the author's knowledge, the investigation of the nucleation (or transformation) process of Zr hydride in HCP Zr matrix using atomistic simulation is still a few. The direct calculation of the nucleation (or transformation) activation energies of Zr hydrides and atomic arrangement during the nucleation or transformation process seems to be effective by detecting the minimum energy path (MEP) of the nucleation or transformation [11]. Nonetheless, such research is scarce, and researchers mainly focus on the investigation of the formation energy, elastic constants, lattice parameters of Zr hydrides, and hydrogen diffusivity [12–15]. Related to the nucleation process of Zr hydrides, recently, using MD simulation with a charge-optimized many-body potential, Zhang et al. discussed the transformation of Zr hydrides from the formation energy and the stacking fault energy change of HCP-FCT phase transformation for ζ hydride [10]. Using DFT calculations, Njifon and Torres calculated the activation energy of the homogeneous transformation from HCP to FCT ζ hydride using MEP detection [16].

In this study, considering the nucleation process of Zr hydrides as HCP-FCT transformation, we calculated the activation energy of the homogeneous nucleation and atomic arrangement during the nucleation process by detecting the MEP of the Zr hydride nucleation using DFT calculations. Zr_4H, Zr_2H (ζ), ZrH (γ) and ZrH_2(ϵ) were employed as the compositions of Zr hydrides and the activation energies of homogeneous HCP-FCT phase transformation were calculated for each composition. By comparing their activation energies, we discuss the mechanism of the nucleation and transformation processes of the Zr hydrides. Additionally, the chemical potential and eigenstrains (or misfit strains) for each Zr hydride are provided because these properties are useful data for the subsequent meso-scale analysis of Zr hydrides [17,18].

E-mail address: ishii@me.es.osaka-u.ac.jp.

https://doi.org/10.1016/j.commatsci.2022.111769
Received 31 July 2022; Accepted 23 August 2022
Available online 7 September 2022

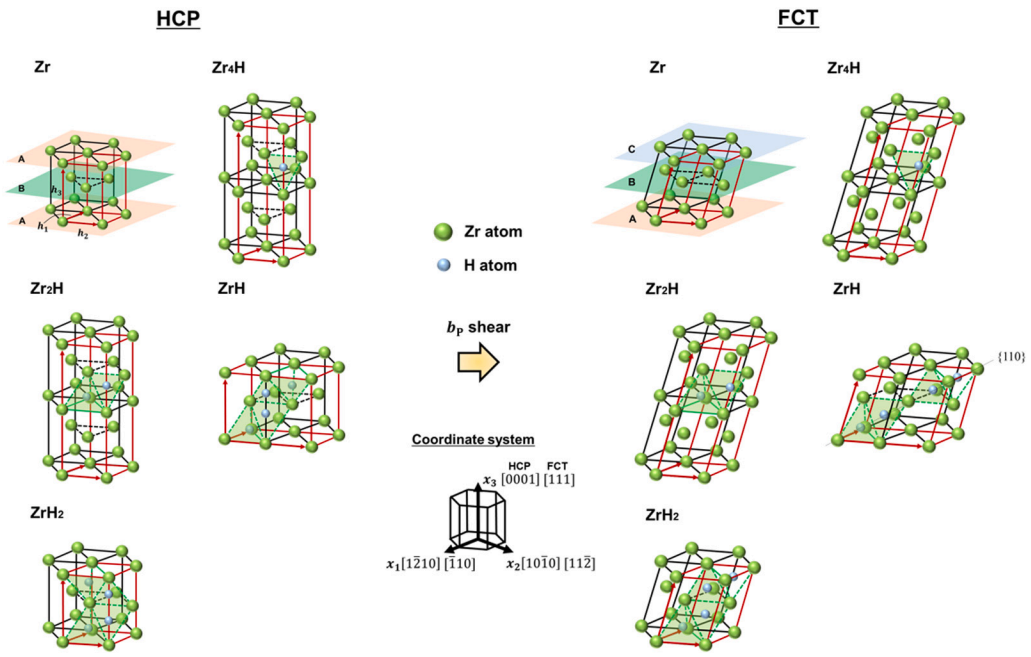

Fig. 1. Atomic structures of pure Zr and Zr hydrides for DFT calculation (HCP and FCT). The supercells used for DFT calculation are shown by red lines and the edge vectors ($\boldsymbol{h}_1$, $\boldsymbol{h}_2$ and $\boldsymbol{h}_3$) of the supercells are shown as red arrows. Green lines are guides for the eye to understand the position of the T-sites and several planes of the tetrahedron of T-sites are shown as translucent green planes to clarify the position of hydrogen.

In Fig. 1, we show the atomic structures (supercells) of HCP and FCT for each composition used in our DFT calculation. Because HCP structures have an ABABAB… basal stacking sequence, and FCT structures have an ABCABC… {111} stacking sequence, The FCT ABCABC… {111} stacking sequence can be considered as an HCP ABABAB… basal stacking sequence with basal plane stacking faults at every other basal plane [7,16,18]. From this crystallographic relationship between HCP and FCT, we consider FCT supercells to be sheared HCP supercells, applying $\boldsymbol{b}_\mathbf{P} = 1/3\langle 10\bar{1}0\rangle$, the Burgers vector of one of the Shockley partial dislocations. Regarding the arrangement of hydrogen atoms, we used a two-atom supercell for pure Zr and ZrH_2 and double-sized four-atom supercells for Zr_4H, Zr_2H and ZrH to describe the stable hydrogen site occupation (see Fig. 1). In both HCP and FCT Zr, DFT calculations revealed that hydrogen atoms exhibit a preferential occupancy at tetragonal sites (T-sites) [8]. The most energetically stable hydrogen arrangement at 0 K for Zr_2H is that in which hydrogen atoms are in neighboring T-sites, forming hydrogen atom layers in HCP [8,9]. The most energetically stable hydrogen arrangement at 0 K for ZrH is that in which all the hydrogen atoms are placed on almost linearly aligned T-sites on the {110} plane. For ZrH_2, all the T-sites in the FCT are occupied by hydrogen atoms [8,19]. We employed these hydrogen arrangements by inserting two hydrogen atoms into the T-sites in the four-atom pure HCP Zr supercells for Zr_2H and four hydrogen atoms in the four- and two-atom pure FCT Zr supercells for ZrH and ZrH_2, respectively. Zr_4H was obtained by removing one hydrogen atom from Zr_2H. FCT Zr_4H and Zr_2H supercells were obtained by shearing HCP supercells $\boldsymbol{b}_\mathbf{P}$, whereas HCP ZrH and ZrH_2 supercells were obtained by shearing FCT supercells $-\boldsymbol{b}_\mathbf{P}$. We then optimized the supercell shape and atomic structure for all HCP and FCT Zr hydrides using DFT calculations. Note that, although $ZrH_{1.66}(\delta)$ is the most frequently observed Zr hydride in experiments [1], it was not investigate here because the details of hydrogen atom arrangements in $ZrH_{1.66}$ are still unclear and DFT calculations are computationally expensive owing to their very large supercell structure.

Employing structurally optimized HCP and FCT supercells for each composition as the initial and final states, we implemented MEP detection of the homogeneous nucleation (HCP-FCT transformation) of Zr hydrides. As an initial guess for MEP, HCP (initial state) and FCT (final state) structures were linearly interpolated, and nine intermediate states were produced with equal intervals along the path. In this study, we refer to these intermediate states as reaction coordinates $\lambda = 0$ (initial HCP), 1, 2, …, and 10 (final FCT), following the previous research in [11,16]. The drag method [11] was used to detect the MEP, constraining the intermediate states on hyperplanes, where the normal corresponds to the tangent of the nucleation path during the optimization to obtain MEP. Note that the shape of the supercell was also optimized.

For DFT calculations, we employed the Vienna *ab*-initio simulation package (VASP) [20]. The electron–ion interaction in DFT is described using the projector-augmented wave method [21] and the exchange–correlation between electrons is treated using the Perdew–Wang generalized gradient approximation in the PW91 functional [22]. An energy cutoff of 350 eV was used for the plane-wave expansion. A $15 \times 15 \times 15$ k-point mesh was used for HCP Zr and ZrH_2, whereas a $15 \times 15 \times 8$ k-point mesh was used for Zr_4H and Zr_2H. A $15 \times 8 \times 15$ k-point mesh was used for the ZrH. The energy convergence criteria for the electronic and ionic structure relaxations were set to 10^{-8} and 10^{-4} eV, respectively. Subroutines for atomic and supercell shape optimization under constraints (drag method) were implemented in the VASP code. Note that our MEP detection is under stress-free conditions, and the finite-temperature configurational entropic effect due to the hydrogen arrangement is ignored.

In addition, we calculated the chemical potentials $\Delta\mu_{Zr_xH_y}$ and eigenstrains (or misfit strains) $\epsilon_{ij}^{Zr_xH_y}$ of Zr hydride Zr_xH_y as follows.

$$\Delta\mu_{Zr_xH_y} \equiv \frac{1}{V^{\mathrm{FCT}}_{Zr_xH_y}}\left(E^{\mathrm{FCT}}_{Zr_xH_y} - a\left(E^{\mathrm{HCP}}_{Zr} + \frac{y}{x}E_{H_2}\right)\right), \tag{1}$$

where $E^{\mathrm{FCT}}_{Zr_xH_y}$ and $V^{\mathrm{FCT}}_{Zr_xH_y}$ are the potential energy (the total energy of the supercell) and volume of the supercell of Zr hydride Zr_xH_y at 0 K, respectively. E^{HCP}_{Zr} and E_{H_2} are the potential energies of pure Zr and hydrogen molecules at 0 K. All values were calculated using DFT calculations. The constants where chosen such that $a = 1$ for pure Zr and ZrH_2, and $a = 2$ for Zr_4H, Zr_2H and ZrH to match the number of zirconium and hydrogen atoms between $E^{\mathrm{FCT}}_{Zr_xH_y}$ and $\left(E^{\mathrm{HCP}}_{Zr} + \frac{y}{x}E_{H_2}\right)$ terms. This is because the supercell sizes of Zr_4H, Zr_2H and ZrH are

Table 1
Calculated activation energy for the HCP-FCT transformation of Zr and Zr hydrides (ΔE_X), chemical potential and eigenstrains of each Zr hydride at 0K. The units of activation energy and chemical potentials are eV/nm^3. $\epsilon_{ij} = \epsilon_{ji}$ and the values of other ϵ_{ij} not listed are zeros. Super- or sub-script X denotes the composition of Zr hydride.

Zr hydride	ΔE_X	$\Delta\mu_X$	ϵ^X_{11}	ϵ^X_{22}	ϵ^X_{33}	ϵ^X_{12}
Zr	2.46	1.7	−0.009	−0.009	0.074	0.177
Zr_4H	1.22	−5.1	0.000	0.004	0.092	0.182
Zr_2H	1.30	−12.5	0.014	0.013	0.101	0.184
ZrH	2.90	−32.3	0.000	0.071	0.166	0.257
ZrH_2	8.81	−61.8	0.100	0.010	0.096	0.119

double those of the HCP pure Zr. Using the optimized supercell matrices of the HCP Zr, $\boldsymbol{H}^{\mathbf{HCP}}_{\mathbf{Zr}}$ and FCT Zr hydrides, $\boldsymbol{H}^{\mathbf{FCT}}_{\mathbf{Zr_xH_y}}$ [7,18], $\epsilon_{ij}^{Zr_xH_y}$ for Zr hydrides was computed in the form of Green strain as

$$\epsilon_{ij}^{Zr_xH_y} = \frac{1}{2}(\boldsymbol{J}^{\mathrm{T}}_{\mathbf{Zr_xH_y}}\boldsymbol{J}_{\mathbf{Zr_xH_y}} - \boldsymbol{I}), \tag{2}$$

where $\boldsymbol{J}^{\mathrm{T}}_{\mathbf{Zr_xH_y}} = \boldsymbol{H}^{\mathbf{FCT}}_{\mathbf{Zr_xH_y}}\left(\boldsymbol{H}^{\mathbf{HCP}}_{\mathbf{Zr}}\right)^{-1}$ denotes the deformation tensor. Note that, using the edge vectors of the supercell, $\boldsymbol{h_1}, \boldsymbol{h_2}$ and $\boldsymbol{h_3}$ (see Fig. 1), a certain cell matrix $\boldsymbol{H}$ is defined as $\boldsymbol{H} \equiv [\boldsymbol{h_1}\ \boldsymbol{h_1}\ \boldsymbol{h_3}]$.

Fig. 2 shows the change in potential energy at each reaction coordinate along the MEP for pure Zr and each Zr hydride composition, as a result of MEP detection. The reference state of the potential energy for each case is the optimized HCP structure (initial state). The atomic configurations at each reaction coordinate are also available in the supplemental material in the CFG format [23]. The curve maximum of the potential energy change shown in Fig. 2 (saddle point) corresponds to the activation energy of HCP-FCT phase transformation at 0 K. The values of the activation energies for each Zr hydride composition are listed in Table 1 together with the chemical energies and eigenstrains. Interestingly, Table 1 shows that Zr_4H and Zr_2H have a lower nucleation activation energy (that of Zr_4H is the lowest), although ZrH and ZrH_2 have much lower chemical potentials and are more energetically stable than the latter. However, ZrH and ZrH_2 have very high activation energies, even higher than those of pure Zr. This indicates that the HCP-FCT transformation occurs earlier, and the hydrogen concentration increases in Zr hydrides after the phase transformation (possibly due to hydrogen diffusion) to form ZrH (γ) or $ZrH_{1.66}$ (δ), stabilizing Zr hydrides at low temperatures. Because ZrH_2 has a lower chemical energy and relatively lower eigenstrain as well (see ϵ_{12} component in Table 1), the increase in hydrogen concentration in Zr hydrides can stabilize the Zr hydrides both chemically and elastically.

To determine the reason for the trend of the activation energies, we show the atomic configurations at reaction coordinate $\lambda = 5$ (middle state): atomic rearrangement during HCP-FCT phase transformation for each Zr hydride composition in Fig. 3. As HCP-FCT phase transformation progresses (i.e. ϵ_{12} increases), hydrogen atoms are observed to have an affine movement as other zirconium atoms for Zr_4H and Zr_2H cases. On the other hand, for ZrH and ZrH_2 cases, not only the affine-like motion, but also non-affine shuffling is necessary for the hydrogen to reach the T-site in the final FCT structure. This extra shuffling process is the reason for the high activation energies of ZrH and ZrH_2 cases.

Next, to investigate the effect of temperature on the activation energies of Zr hydride nucleation, we calculated the free energy at each state along MEP, $F_X(\lambda, T)$, including the effect of the vibration entropy (phonon), as follows.

$$F_X(\lambda,T) \equiv E_X(\lambda) + \int_0^\infty \rho_X(\omega,\lambda)\left(\frac{1}{2}\hbar\omega + k_BT\ln\left[1-\exp\left(-\frac{\hbar\omega}{k_BT}\right)\right]\right)\mathrm{d}\omega, \tag{3}$$

where $E_X(\lambda)$ is the potential energy at λ for Zr hydride composition X from DFT calculations (note $E_X(0) = E_X^{\mathrm{HCP}}$ and $E_X(10) = E_X^{\mathrm{FCT}}$). ω is the phonon frequency, and ρ is the phonon density of state (DOS). T is the temperature, k_B is the Boltzmann constant, and $\hbar$ is the reduced Planck constant. Employing Phonopy software [24],

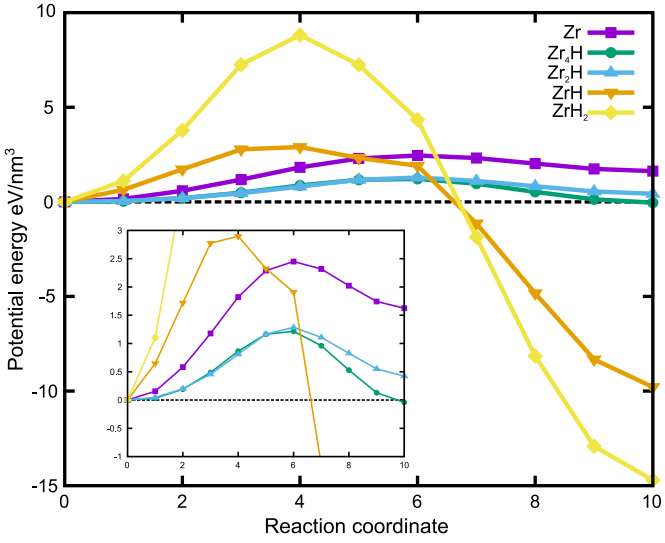

Fig. 2. Potential energy change along MEP during HCP-FCT phase transformation for pure Zr and Zr hydrides.

ρ and the atomic displacement of each phonon mode were obtained using the force constants, which were calculated using the density functional perturbation theory. A 20 × 20 × 20 q-point mesh was used for HCP Zr and ZrH_2. A 20 × 20 × 10 q-point mesh was used for Zr_4H and Zr_2H. A 20 × 10 × 20 q-point mesh was used for the ZrH. As a result, in Fig. 4, we show (a) free energy change along MEP at 300 K (as an example) and (b) temperature versus activation energy plot for pure Zr and Zr hydrides. Interestingly, although Zr_4H and Zr_2H have a lower activation energy at 0 K limit, under finite temperature conditions, the crossover of the activation energies occurs around 300 K, and ZrH becomes the most possible candidate with the lowest activation energy. The increase in the activation energy with respect to temperature for Zr_4H and Zr_2H was relatively higher than that of ZrH and ZrH_2. It is well known that several phonon modes of the system are lost (the frequency becomes negative) during phase transformation [25]. This causes an increase in the activation energy at a finite temperature from the second term in the integration of Eq. (3). We found that the crossover is due to the frequency difference of the lost phonon modes during the HCP-FCT phase transformation between Zr hydride compositions. From our phonon analysis, affine-like motion with low frequency, in which zirconium and hydrogen atoms move together, was found as lost phonon mode at the middle states of the phase transformation for Zr_4H and Zr_2H. On the other hand, hydrogen atom shuffling (without the movement of zirconium atoms) with high frequency was found to be the lost phonon mode for ZrH and ZrH_2. For a clearer understanding, the reader can refer to our supplemental movie: the atomic displacement of the phonon mode with negative frequency (at the gamma point) for $Zr_2H(\zeta)$ and ZrH (γ) hydrides. From Eq. (3), the lower-frequency mode reduces the free energy of the stable state more; $\ln\left[1-\exp\left(-\hbar\omega/k_BT\right)\right]$ becomes more negative; thus, the loss increases the temperature effect on the activation energy, causing the crossover of the activation energy at a finite temperature between the Zr hydrides. Additionally, the decrease in the activation energy of ZrH with respect to temperature may be due to the change in the phonon distribution between the initial and saddle states [25]. The phonon modes with high frequency increase during the phase transformation compared to the initial HCP state for ZrH. For more details, the reader is invited to compare the cumulative phonon DOS ($P_X(\bar{\omega},\lambda) = \int_0^{\bar{\omega}}\rho_X(\omega,\lambda)\mathrm{d}\omega / \int_0^\infty \rho_X(\omega,\lambda)\mathrm{d}\omega$) of ZrH at $\lambda = 0$ and $\lambda = 5$ in the Supplementary Material.

In summary, we calculated the activation energy of the homogeneous nucleation process for Zr hydrides and atomic rearrangement

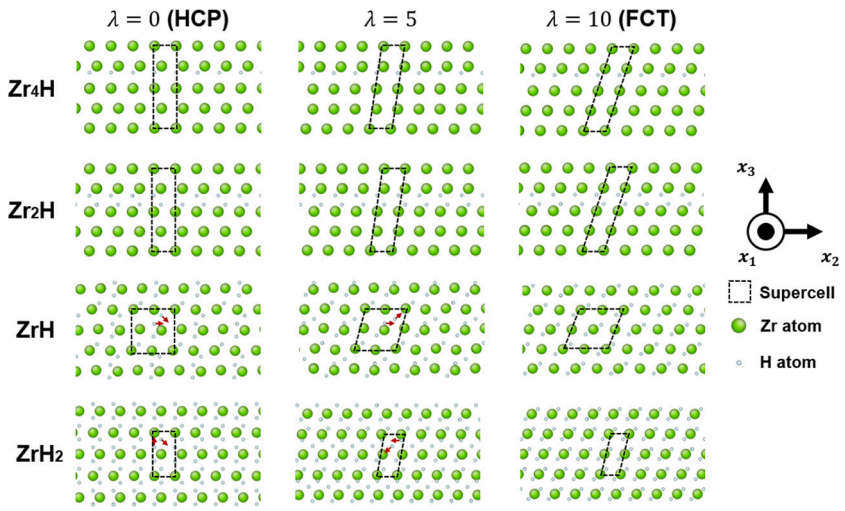

Fig. 3. Atomic configurations of Zr hydrides at certain reaction coordinate λ in Fig. 2. The red arrows in ZrH and ZrH_2 indicate the direction of the hydrogen shuffling during HCP-FCT phase transformation. The atomic structures are visualized using AtomEye [23].

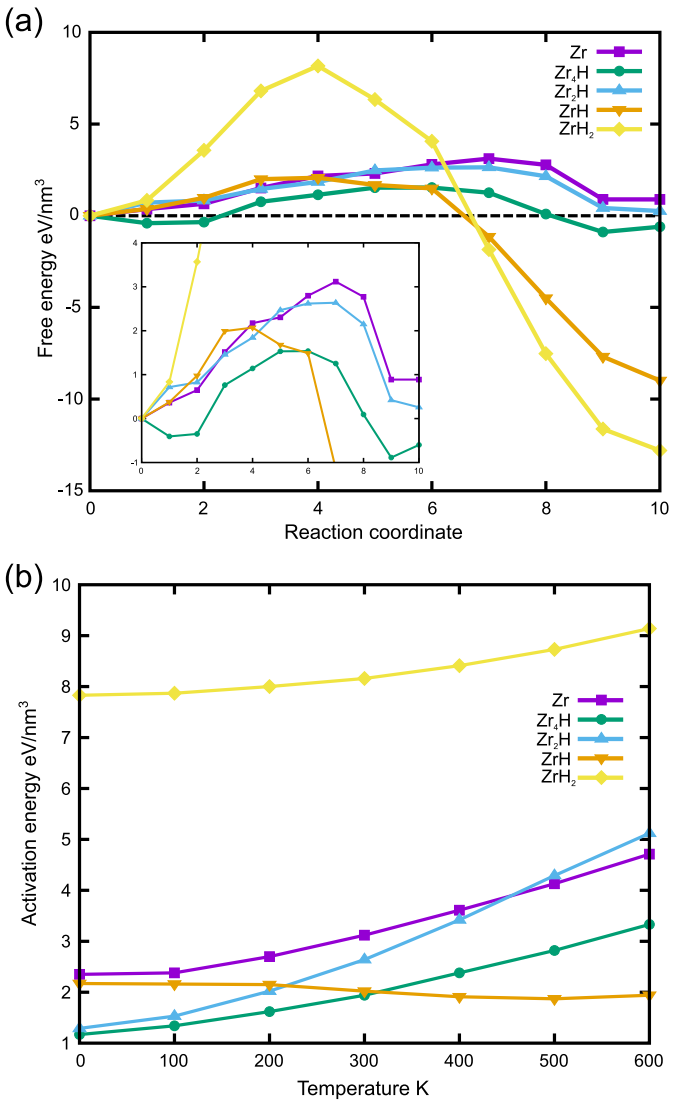

Fig. 4. (a) Free energy change along MEP during HCP-FCT phase transformation for pure Zr and Zr hydrides at 300 K. (b) Temperature versus activation energy plot.

during nucleation for Zr_4H, Zr_2H, ZrH and ZrH_2 using DFT calculations and MEP detection (drag method), considering the nucleation process of Zr hydrides as a phase transformation from HCP to FCT structure. Although ZrH and ZrH_2 have lower chemical potentials and are more energetically stable than Zr_4H and Zr_2H, at the 0 K limit, Zr_4H and Zr_2H have lower activation energies for nucleation. The high activation energies for ZrH and ZrH_2 were attributed to the extra non-affine shuffling of hydrogen atoms during HCP-FCT transformation. On the other hand, at a finite temperature, crossover of the activation energies occurs around 300 K, and ZrH becomes the most possible candidate with the lowest activation energy. This is mainly due to the difference in the frequency of the lost phonon modes during the phase transformation. The affine-like phase transformation for Zr_4H and Zr_2H lost the low frequency modes, whereas shuffling-like phase transformation for ZrH and ZrH_2 lost the modes with high frequency.

Declaration of competing interest

The authors declare that they have no known competing financial interests or personal relationships that could have appeared to influence the work reported in this paper.

Data availability

Data will be made available on request.

Acknowledgments

This study was partially supported by a Grant-in-Aid for Scientific Research (C) 21K03771 from the Japan Society for the Promotion of Science (JSPS). DFT simulations were partly performed using OCTOPUS large-scale computer systems at the Cybermedia Center, Osaka University.

Appendix A. Supplementary data

Supplementary material related to this article can be found online at https://doi.org/10.1016/j.commatsci.2022.111769.

References

[1] A.T. Motta, L. Capolungo, L.Q. Chen, M.N. Cinbiz, M.R. Daymond, D.A. Koss, E. Lacroix, G. Pastore, P.C.A. Simon, M.R. Tonks, B.D. Wirth, M.A. Zikry, J. Nucl. Mater. 518 (2019) 440–460.

[2] A.A. Plyasov, V.V. Novikov, Y.N. Devyatko, Phys. Atomic Nucl. 83 (2020) 1407–1424.

[3] D.O. Northwoodkosasih, Int. Met. Rev. 28 (1983) 92–121.

[4] C.E. Ells, J. Nucl. Mater. 28 (1968) 129–151.

[5] J. Bair, M. Asle Zaeem, M. Tonks, J. Nucl. Mater. 466 (2015) 12–20.

[6] G.J. Carpenter, J.F. Watters, J. Nucl. Mater. 73 (1978) 190–197.

[7] S.M. Liu, A. Ishii, S.B. Mi, S. Ogata, J. Li, W.Z. Han, Small 18 (2022) 2105881.

[8] M. Christensen, W. Wolf, C. Freeman, E. Wimmer, R.B. Adamson, L. Hallstadius, P.E. Cantonwine, E.V. Mader, J. Phys. Condens. Matter. 27 (2015) 025402.

[9] Z. Zhao, J.P. Morniroli, A. Legris, A. Ambard, Y. Khin, L. Legras, M. Blat-Yrieix, J. Micro. 232 (2008) 410–421.

[10] Y. Zhang, X.M. Bai, J. Yu, M.R. Tonks, M.J. Noordhoek, S.R. Phillpot, Acta Mater. 111 (2016) 357–365.

[11] H. Jonsson, G. Mills, K.W. Jacobsen, in: B.j. berne, g. ciccotti, d.f. coker (Eds.), Classical and Quantum Dynamics in Condensed Phase Simulations, World Scientific, Singapore, 1998.

[12] P. Olsson, A. Massih, J. Blomqvist, A.-M. Alvarez Holston, C. Bjerkén, Comput. Mater. Sci. 86 (2014) 211–222.

[13] Y. Zhang, C. Jiang, X. Bai, Sci. Rep. 7 (2017) 41033.

[14] X. Zhu, D.Y. Lin, J. Fang, X.Y. Gao, Y.F. Zhao, H.F. Song, Comput. Mater. Sci. 150 (2018) 77–85.

[15] C.M. Andolina, W.A. Saidi, H.P. Paudel, D.J. Senor, Y. Duan, Comput. Mater. Sci. 209 (2022) 111384.

[16] I.C. Njifon, E. Torres, Acta Mater. 202 (2021) 222–231.

[17] G. Han, Y. Zhao, C. Zhou, D.-Y. Lin, X. Zhu, J. Zhang, S. Hu, H. Song, Acta Mater. 165 (2019) 528–546.

[18] A. Ishii, Comput. Mater. Sci. 211 (2022) 111500.

[19] C. Domain, R. Besson, A. Legris, Acta Mater. 50 (2002) 3513–3526.

[20] G. Kresse, J. Furthmüller, Phys. Rev. B 54 (1996) 11169–11186.

[21] G. Kresse, D. Joubert, Phys. Rev. B 59 (1999) 11–19.

[22] J. Perdew, J. Chevary, S. Vosko, Phys. Rev. B 46 (1992) 6671–6687.

[23] J. Li, Modell. Simul. Mater. Sci. Eng. 11 (2003) 173–177.

[24] A. Togo, I. Tanaka, Scr. Mater. 108 (2015) 1–5.

[25] C.P. Flynn, Point Defects and Diffusion, Clarendon Press, 1972.